



**Determination of the microscopic mineralogy of inclusion in
an amygdaloidal pillow basalt by fs-LIMS**

Journal:	<i>Journal of Analytical Atomic Spectrometry</i>
Manuscript ID	Draft
Article Type:	Paper
Date Submitted by the Author:	n/a
Complete List of Authors:	<p>Tulej, Marek; University of Bern, Physics Institute; Lukmanov, Rustam; Universitat Bern Philosophisch-naturwissenschaftliche Fakultat Grimaudo, Valentine; University of Bern Physics Institute Riedo, Andreas; University of Bern Faculty of Natural Sciences, Physics Institute de Koning, Coenraad; University of Bern, Space Research and Planetary Science, Physics Institute Ligterink, Niels; Universitat Bern Philosophisch-naturwissenschaftliche Fakultat Neubeck, Anna; Department of Geological Sciences, Uppsala University Ivarsson, Magnus; Department of Paleobiology, Swedish Museum of Natural History Wurz, Peter; University of Bern, Physics Institute</p>

ARTICLE

Determination of the microscopic mineralogy of inclusion in an amygdaloidal pillow basalt by fs-LIMS

Received 00th January 20xx,

Accepted 00th January 20xx

DOI: 10.1039/x0xx00000x

Marek Tulej,^{† a} Rustam Lukmanov^a, Valentine Grimaudo^a, A. Riedo^a, Coenrad de Koning^a, Niels F. W. Ligterink^b, Anna Neubeck^c, Magnus Ivarsson^d and Peter Wurz^a

We present chemical depth profiling studies on mineralogical inclusions embedded in amygdale calcium carbonate by our Laser Ablation Ionisation Mass Spectrometer designed for in situ space research. An IR femtosecond laser ablation is employed to generate ions that are recorded by a miniature time-of-flight mass spectrometer. The mass spectra were measured at several locations on the sample surface and yield chemical depth profiles along the depth length of about 30 μm . The presence of oxides and sulphides within inclusion material allows us to derive elemental abundance calibration factors (relative sensitivity coefficients, RSCs) for major and minor elements. These are obtained from the atomic intensity correlations performed on the depth profiling data. With the RSCs corrections the quantitative analysis of more complex mineralogical phases within the inclusion is conducted by correlating atomic abundance fractions in ternary diagrams, typically used in geology. The spatial resolution of the depth profiles was sufficient to study chemically distinct micrometre-sized objects, such as mineralogical grains and thin layers of minerals including micrometre-sized filamentous structures. The method presented here is well-suited for the quantitative chemical analyses of highly heterogeneous materials where the ablation condition can vary locally with the material composition making the application of standard reference materials less accurate. The presented method is developed to distinguish between abiotic and biological material while searching for micrometre-sized extinct or extant life forms on the surfaces of Solar System bodies.

Introduction

One of the major objectives of current space research and planetology is the search for signatures of extant and extinct life on other planetary bodies. With the assumption that life on other planets should be based on the same physical and chemical rules as life we know from Earth and evolved along similar pathways, these searches should follow known terrestrial practice. Ancient extinct life can be identified by finding remains of organic material, stromatolitic layers, and individual microfossils within planetary rocks and soils¹. Identification of metabolic products together with the

deciphering of fossilization mechanisms can be essential in such searches. Among available analytical instrumentation, only these instruments, which can deliver selective and sensitive chemical measurements of microstructures can be employed for this task^{2,3}.

For conducting analyses on planetary bodies only small, light, low-powered and sufficiently robust instrumentation can be used. Several space-borne instruments including Laser-Induced Breakdown Spectroscopy (LIBS), X-Ray Fluorescence (XRF), and Laser Raman Spectroscopy have proved their capabilities in delivering composition measurements of the sample

^a Space Research and Planetary Sciences, Physics Institute, University of Bern Switzerland.

^b Centre for Space and Habitability, University Bern, Switzerland

^c Department of Geological Sciences, Uppsala University, Sweden.

^d Department of Paleobiology, Swedish Museum of Natural History, Sweden.

[†] Corresponding author: marek.tulej@space.unibe.ch

Electronic Supplementary Information (ESI) available: [details of any supplementary information available should be included here]. See DOI: 10.1039/x0xx00000x

1
2
3 surface and important biosignatures in numerous
4 performance studies. However, their measurement
5 sensitivity might not be sufficient to investigate the
6 chemical composition of microstructures of sparse life².
7
8 ³. An example of the instrument combining Raman, LIBS
9 and IR techniques is the SuperCam instrument designed
10 on the NASA Mars2020 with the performance figures of
11 each of applied technique described in recent
12 publication and references therein^{4, 5}. Compared to
13 these techniques, laser-based mass spectrometry adds
14 complementary information. With current LIMS spatial
15 resolution (lateral and vertical) and sensitivity, detailed
16 analyses of grain-size objects can be conducted with the
17 determination of context mineralogy and detection of
18 micro-sized fossils⁶⁻⁸.

22
23 Laser ablation ionisation mass spectrometry (LIMS)
24 based on time-of-flight mass analysers is a well-known
25 technique with its origin in the mid-1970s. In the
26 beginning, the technique suffered from various
27 drawbacks, which mostly were affecting the
28 quantification and the measurement procedure. With
29 the continuous advances in electronics, vacuum, and
30 laser systems, this technology has re-emerged for
31 laboratory and field application for chemical analysis of
32 solid-state samples⁹⁻¹¹. Over the years, a high degree of
33 miniaturisation of the LIMS instrument has been
34 achieved with the objective to become a space-borne
35 instrument^{7, 12-14}. Robustness of time-of-flight mass
36 analyser, flexible operation of the laser ablation ion
37 source, the control over the ion optics settings and
38 detector gain allow direct and sensitive chemical
39 analysis of raw samples providing efficient ion
40 production and nearly 100% ion transmission from the
41 measurement spot to ion detector^{14, 15}. For the analysis
42 of micro-sized objects such as grains or microfossils, the
43 integration of a microscope camera system into the
44 system helps in an initial characterisation of micro-sized
45 objects and improving overlap of the laser spot with the
46 object of interest^{7, 16}.

51
52
53
54
55 LIMS with an fs laser ablation ion source shows an
56 increasingly higher performance. It delivers improved
57 quantitative chemical composition information with
58 considerably reduced element fractionation¹⁷⁻¹⁹. Several
59
60

recent studies show that LIMS can be considered as a
standardless technique delivering semi-quantitative
results¹⁷⁻²¹. Further improvements to the quantitative
analysis can be achieved by adding to atomic abundance
derived from the single-charged atomic mass peaks also
multiple ionised atomic mass peaks²². An improved
efficiency of the atomic ion production and
quantification of atomic ions can be achieved applying a
double pulse laser ablation/ionisation ion source²³. In
double pulse system, the first pulse is ablating the
sample surface and the second, shortly delayed pulse
interacts with freshly formed plasma plume resulting in
additional plasma heating, atomisation and ionisation.
These processes influence also post-plasma chemistry
efficiency. The presence of isobaric multiple-charged
atomic ions and clusters in ion beam can introduce
uncertainty in the quantification of the atomic signal
measurement; hence, by applying double pulse laser ion
source, the isobaric interferences can be minimized. It
has been demonstrating also that the isobaric
interferences due to clusters could be reduced by
implementing collisional cell which allows partial
temporal separation of the cluster and atomic ion
distributions²⁴. High-resolution time-of-flight mass
spectrometric measurements of atomic ions produced
in laser ablation are typically difficult due to wide kinetic
energy distributions of produced ions. Only, recently a
high-resolution ($M/\Delta M \sim 10^4$) laboratory LIMS system
with a double reflectron system was developed to
resolve most of mass peaks of cluster ions, hence, the
isobaric interferences resulting from polyatomic species
can be avoided²⁵. In miniature LIMS systems designed
for in situ applications not all these implementations can
be made. Here, we propose alternative method of the
abundance calibration. The applied method uses depth-
profiling data and requires presence of simple chemical
compounds such as oxides and sulphides within the
sample material.

In recent years, fs-LIMS proved its capabilities for
chemical analysis with high spatial (lateral, vertical)
resolution. High lateral resolution is achieved by
focusing laser radiation onto the surface to a spot size of
a few micrometres and by tuning over the pulse energy,

ablation rate and thickness of the ablated layer can be well controlled so that the measurements can be conducted with the depth resolution down to a few nanometres^{26, 27, 28, 29-31}. In our recent studies on the Ni/Cr NIST standard, we have accomplished a depth resolution of about 30 nm applying UV femtosecond laser radiation arranged in a double pulse configuration^{23, 31}. 3D chemical mapping analysis with LIMS were recently presented^{32, 33}.

There are other laboratory analytical techniques, which offer high spatial resolution depth profiling capabilities such as Glow Discharge Mass Spectrometry (GD-MS), Laser Ablation Inductively Coupled Mass Spectrometry (LA-ICP-MS) and Secondary Ion Mass Spectrometry (SIMS)³⁴⁻³⁹. These instruments in current state of development are less suitable for application to space research but can be useful in applications in terrestrial environments. Current LIMS systems fulfil the requirements of size, weight or power consumption necessary available aboard a spacecraft, either a rover or a lander⁷.

In the current contribution, we introduce a procedure for the in-situ atomic abundance calibration using micro-sized inclusion embedded in calcium carbonate mineral. The procedure uses the depth profiling data e.g. the measurements of atomic intensities in a function of ablation layer. By correlating atomic intensities measured at specific ablation layers and observation of linearly correlation, one can determine relative atomic intensities. The presence of the simple chemical compounds such as oxides and sulphides in the sample further comparison between relevant atomic fractions and determination of relative coefficient factors (RSCs). With true elemental abundances, atomic abundance fractions are correlated in ternary diagrams allowing the investigation of more complex mineralogical phases. Similar materials to that studied here are found on Mars and can be considered as a distinct astropaleontological target. The calcium carbonate phase in basalts can host veins and voids, which are recognised as habitats for endolithic microorganisms and form secondary infilling mineralisation in volcanic environments⁴⁰⁻⁴³. Thus,

extended characterisation of these materials and understanding their heterogeneities are important to account for their biological or abiotic origin.

Experimental

Materials

The sample of an amygdaloidal pillow basalt from Kinghorn, Fife, Scotland⁴⁴ was processed to a 30 μm thick thin-section, mounted on a stainless-steel sample holder and introduced into the vacuum chamber for its mass spectrometric analysis (Fig. 1). The left panel of Fig. 1 shows the thin-section of basalt with an inclusion of calcium carbonate. The right panel shows a close-up image of the dark inclusion, which contains a number of needle-shaped microscopic structures. The enclosure into the calcium carbonate host happened some 360–320 Ma ago⁴⁴.

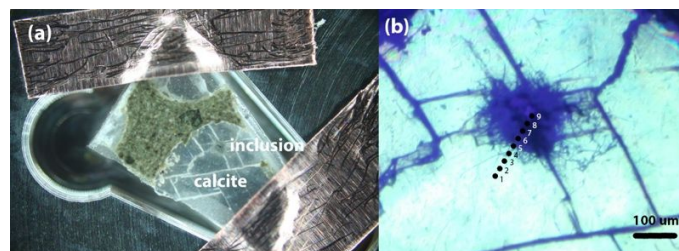


Fig. 1. (a): The sample prior to the introduction into the vacuum chamber. The sample is placed within milled depression in the sample holder made of stainless steel and is attached by a copper tape. (b): Close up microscope image of the amygdale calcium carbonate sample with a dark inclusion in the centre. A network of needle-like structures spreading out from a denser, darker central part of the inclusion can be readily identified. The ten black spots with numbers indicate the location at which laser ablation mass spectrometric analyses were conducted.

The LIMS instrument

The mass spectrometric investigations were conducted with our miniature laser ablation ionisation mass spectrometer designed for in situ space research applications. The instrument combines a femtosecond-laser ablation ion source with a miniature time-of-flight mass analyser²¹. Current studies are conducted with a NIR-fs-laser radiation (pulse width, $\Delta t \sim 190$ fs, $\lambda = 775$ nm, laser pulse repetition rate of 1 kHz) focused to a circular spot of about 10 μm in diameter. In all measurements, a pulse energy of about 8 μJ on the sample surface was applied. The resulting craters were inspected with an optical microscope¹⁶. The detailed crater morphology analyses can be found in our

previous publications³⁰. The measurements were computer-controlled using our custom-designed operating system¹⁴. The sample was attached to the xyz-micro-translation stages. The stage allows for about 2 μm positioning accuracy of the location of interest on the sample by using prior measurements size calibration with an in-situ microscope camera system¹⁶.

Mass spectrometric measurements

Mass spectra were collected at ten locations on the sample, starting from the pure calcium carbonate mineral, across the interface of the calcium carbonate host all the way into the dark inclusion, and on the inclusion's surface seen as a dark area in the centre of Fig. 1b. The dark inclusion consists of needle-shaped micrometre-sized structures that are embedded in complex mineralogical phases other than calcium carbonate. For each location 300 mass spectra were acquired corresponding to 300 ablated layers. The individual layer spectrum is measured by accumulation mass spectra of 200 laser shots on board of the acquisition system. Additionally, mass spectra on the calcium carbonate host were collected by drilling through the 30 μm thin-section, which corresponds to about 366 layers. The mass calibration of the spectra, mass peak integration and principles of depth profiling analysis were discussed in detail in our previous publications^{45, 46}.

Relative sensitivity coefficients

The Relative Sensitivity Coefficients (RSCs) for each element are defined as:

RSC = experimentally measured element concentration / expected element concentration deduced from the chemical formula.

Two methods are applied here to determine RSCs from the experimental data. The first method utilises the direct mass peak integration

$$(1) \quad RSC_X = \frac{A_X / A_{tot}}{P_X}$$

where X is a particular element, A stands for the peak area of the element, A_{tot} is the sum of the peak areas included particular chemical formula of the measured

phase, and P_X denotes the expected fraction of the element X in the measured phase, e.g., the C fraction in pure calcium carbonate, CaCO_3 is 20%. This method is less suitable for determining RSCs of elements present in heterogenous samples. We introduce here new method based on the signal intensity correlation between species forming relatively simple chemical compounds. This second method allows the determination of RSCs from the signal intensity correlation between species in simple chemical compound, e.g., two or three-element compounds such as oxides or sulphides. These compounds while present in the heterogeneous medium can be part of different ablation layers. For the correlation, we select the atomic signals of a compound, which originate from various ablation layers. Atomic signals emerging from the same compound will always create a linear correlation, since the element ratio will stay constant in all different layers, independently of the amount of the compound. The slope of a linearly correlated data set is then the effective abundance ratio of the two correlating atomic species. Knowing RSC of one of the components and the chemical formula, one can determine the RSC of the other component.

Initially RSCs of C, O and Ca are determined from the mass spectrum measured on the calcium carbonate mineral (all individual mass spectra measured along depth are added) by integrating relevant mass peaks to obtain atomic fractions. The results are subsequently compared with those obtained by the intensity correlation method (see Fig.1, panel b, locations 1-4). Similar analysis is conducted on data at the interface between the calcium carbonate phase and inclusion, and at the inclusion (Fig.1, panel b, locations 5-9). With some fraction of calcium carbonate identified at specific ablation layers by the C and Ca, and, O and Ca intensity correlation method also RSC for these elements can be determined considered chemical formula of calcium carbonate. RSC values for other elements are determined from the correlation studies of these elements with O and S considering that they can form sulphides and oxides.

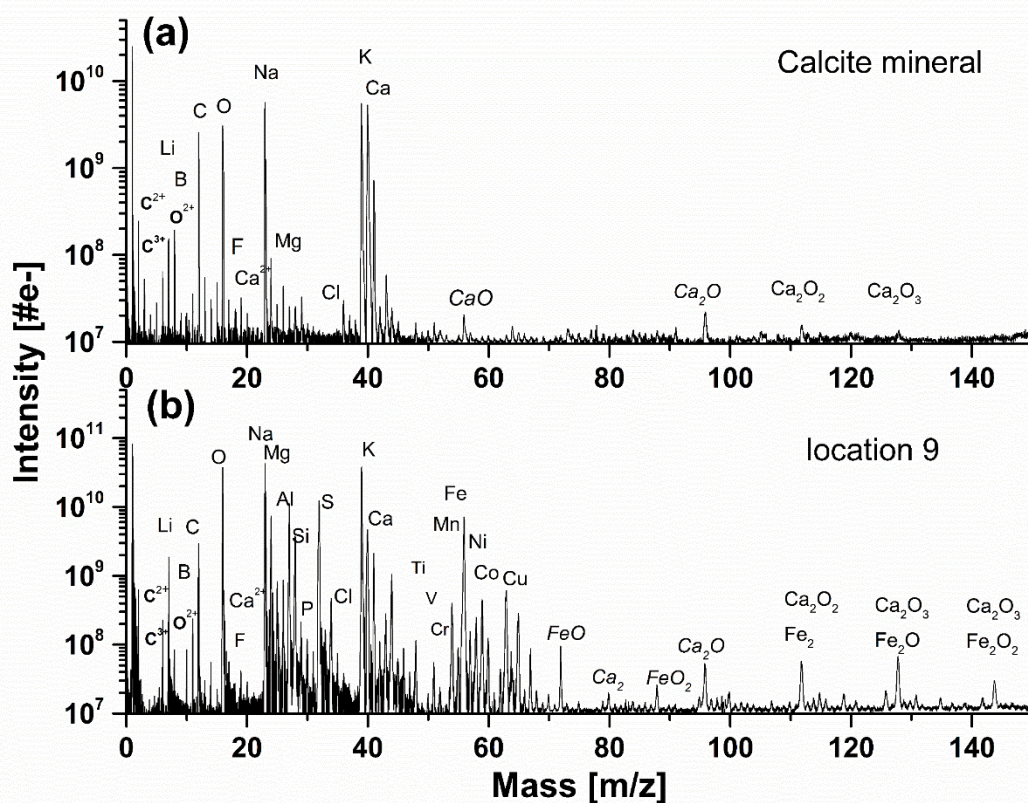


Fig. 2 (a) The mass spectrum recorded on a pure calcium carbonate mineral on location 4, (b) and on the inclusion on location 9.

Results and discussion

Mass spectra of the calcium carbonate phase and the dark inclusion

Figure 2a shows the mass spectrum measured on the pure calcium carbonate with C, O, and Ca as the major elements that are characteristic for the calcium carbonate mineral composition, $CaCO_3$. From purely mass spectrometric perspective, it is hard to identify polymorphic modifications. The calcium carbonate could be calcite, aragonite, or vaterite, but earlier it was determined to be calcite⁶. Additionally, we also observe mass peaks of the elements Na and K. The dynamic range of the spectrum is close to 10^4 , which allowed for simultaneous detection of the major elements and trace elements with a bulk concentration of at least 100 ppm (atomic fractions). In addition to C, O and Ca also Li, B, F, Mg, S, Cl, and Sr elements are identified in the spectrum. These elements are known impurities in the calcium

carbonate minerals. Other mass peaks within the low atomic mass range are double- and triple-charged ions of C, O, and Ca. Non-equilibrium chemistry in the expanding and cooling ablation plume leads to the formation of hydrocarbons, C_xH_y , and oxides, Ca_xO_y (where $x = 1-3$ and $y = 1-4$), which ions are also observed in the mass spectrum. Similar mass spectra are recorded at locations 1-4 (see also Fig. 1b), indicating chemical homogeneity of the host mineral.

The mass spectrum displayed in Fig. 2b was measured on the inclusion at location 9 (see also Fig. 1). The major and minor elements observed are O, Na, K, Fe and C, Mg, Al, Si, S, Ca, Ni, Co, respectively, including also the trace elements, Li, N, P, Ti, V, Cr, Cu, Zn and Sr. The dynamic range in the spectra is larger than 10^4 . An increase of the signal to noise ratio (S/N) at the inclusion location compared to that at the calcium carbonate mineral is attributed to a larger ablation rate due to favourable laser ablation conditions, i.e., better

absorption of the laser radiation by the dark inclusion material. In addition, multiple charged ions, hydrocarbons and oxides of the main constituents C, O, Ca, and Fe can be identified in the mass spectra. The resemblance of the mass spectra at location 9 and at locations 6, 7 and 8 is large, indicating negligible chemical heterogeneity in the dark inclusion. However, the depth profiling analysis shows that the inclusion material is heterogeneous.

Chemical depth profiling on calcium carbonate mineral

Figure 3a shows the chemical depth profiles measured for the elements C, O, Na, and Si along the 30 micrometre-thick calcium carbonate sample as a function of the ablation layer number. The measured mass peak intensities are observed to decrease fast for about first 30 ablation layers and for the remaining ablation layers - approximately monotonically with the ablation layer number. Because of the mass peak shape distortions and peak intensity fluctuations in the spectra recorded during an initial ablation phase (here for the first 30 ablation layers) these spectra are removed from the analysis. Above the ablation layer number 366 we observe a sudden signal increase for all elements, including Na and Si. The Na and Si signals show the transition to the soda lime glass substrate, which indicates that the laser has drilled a crater through approximately 30 μm thick thin-section sample. Approximately circular craters with a diameter of about $\varnothing 10 \mu\text{m}$ were produced as observed with the internal optical microscope¹⁶. More advanced analyses of the crater characteristic were not conducted in the current study.

Mass peak intensity correlation of C, O and Ca

Calcium carbonate mineral

The correlation plot of the mass peak intensities (the peak areas) of C and Ca and O and Ca, respectively, is displayed in Fig. 3, panel b. One observes linear correlations for this data with approximately similar curve slope coefficient as shown in Fig. 3b. The slope coefficients derived from the linear fits are 0.19 ± 0.01 and 0.20 ± 0.02 for the correlation of C with Ca and of O with Ca, respectively. Considering the theoretical

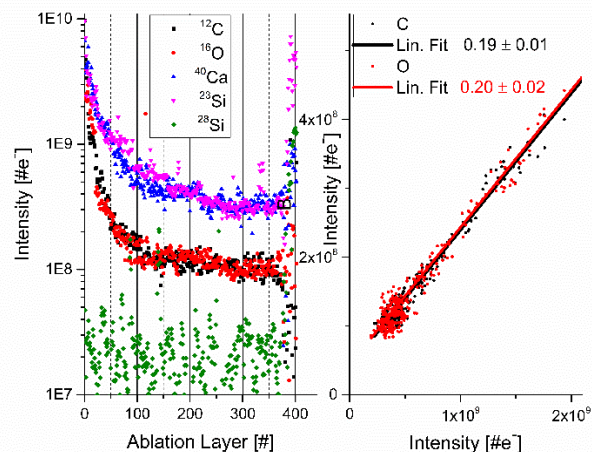


Fig. 3 (a): Depth profile of C, O, Ca, Na, and Si as a function of the ablation number. From the 366 ablation layer one observes an increase of the Si and Na atomic intensities indicating transition to soda lime silica glass substrate material. (b): Correlation between C and Ca, and O and Ca atomic intensities, respectively, derived from the depth profiling data.

abundance of the elements in the pure calcium carbonate mineral, we derive relative sensitivity coefficients, RSCs of 0.20 ± 0.01 , and 0.07 ± 0.03 for C, O, respectively. Here, RSC for Ca is taken as the reference and is equal to 1. Similar RSC values are obtained by the integrating the relevant mass peaks in the spectrum obtained by summed up spectra for the individual ablation layers (Fig. 2a). The RSCs for C and O for these measurements are 0.18 ± 0.03 , 0.12 ± 0.05 , respectively. Again, RSC of Ca is taken as the reference with its value 1. Hence, sufficiently close to each other RSCs values can be obtained using both these methods.

For a sample consisting of heterogeneities within a volume smaller than the sampled volume, the determination of RSC from the mass spectrum at this location would yield inaccurate results, because an unique element composition is assumed for the entire volume, thus entire data set. Using depth profiling, the mass peak intensity correlation method can be applied for each individual layer which yields more accurate results. The specific chemical composition of each layer is preserved and the spatial resolution with the profiling depth is expected to be in sub-micrometre range. In this way an isolation between various compounds can be achieved and the different mineralogical phases are recognised by means of their unique elemental composition (abundance ratio) within the various

(Fig. 4, panel a, see also location 5 in Fig. 1b). Similar

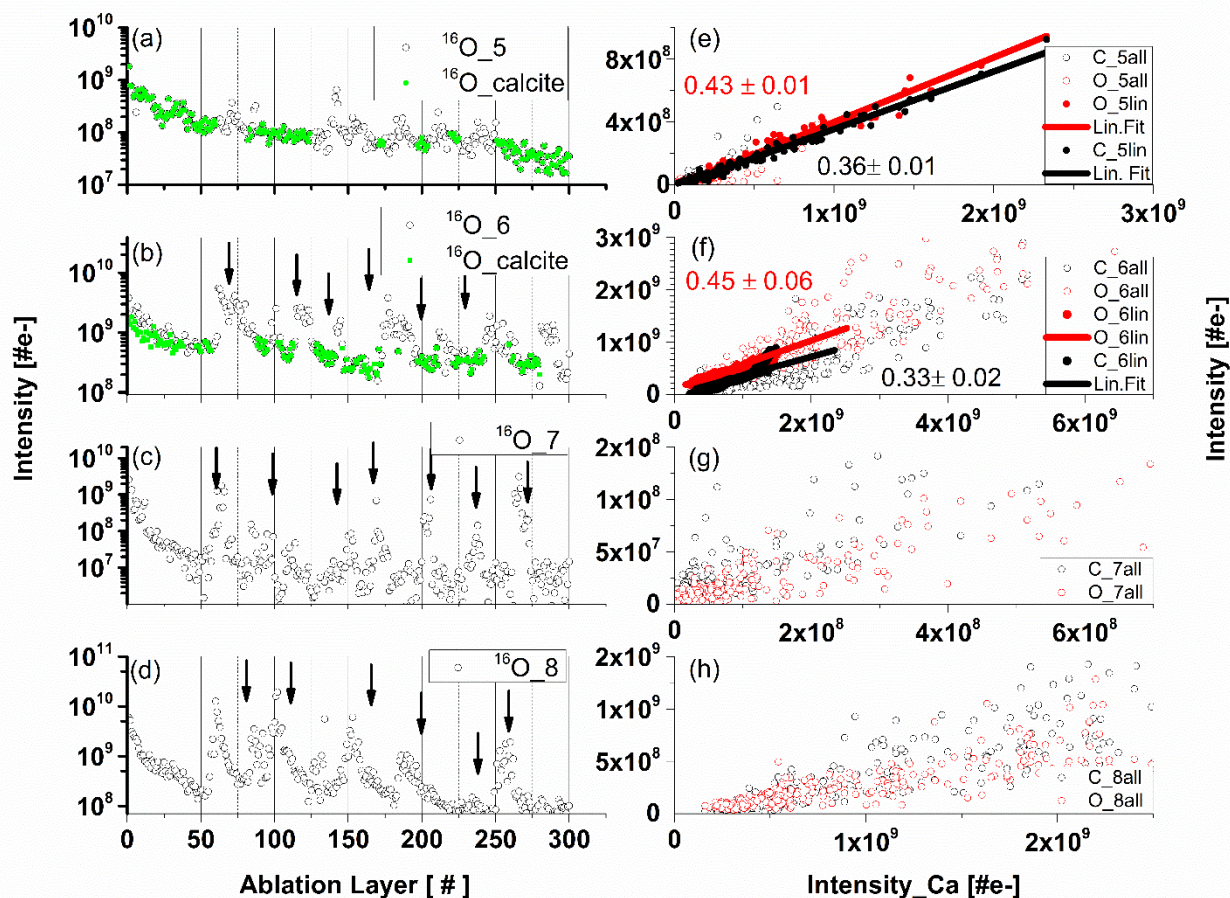


Fig. 4. Depth profiles and mass peak intensity correlations. Panels (a-d): Depth profiles obtained by measuring the O mass peak intensities at the locations 6 panel (b), 7 panel (c), and 9 panel (d) on the dark inclusion. A depth curve on a pure calcium carbonate mineral is added in panel (a) for comparison with depth profiles measured at inclusion locations. The green-coloured points in the left panels are the data points that correspond to the calcium carbonate mineral. Right panels: the correlations of the mass peak intensities of elements C and O (y-axis) with Ca (x-axis) measured at corresponding locations. Only part of the data points correlates linearly (black and red full circles) in panel (f). There was no clear correlation between O and Ca in the data plotted in panel (g), although a C-Ca correlation can be noticed. Contrary, for part of the data points the correlation between O and Ca is readily observed but the correlation between C and Ca is less pronounced in panel (h).

ablation layers. Hence, they can be identified from the correlation studies. Nevertheless, the lateral resolution of this study is at least order of magnitude lower and may affect an isolation of the signals if more than one unique mineralogical grains will be ablated simultaneously.

Inclusion material

Figure 4 compares the O depth profiles in a function of ablation layer number recorded at various locations on the inclusion including also location at the interface between pure calcium carbonate and inclusion material

depth profiles are observed for C and Ca although some differences at specific ablation layers in the profile shapes can be noticed. An increase of mass peak intensities at specific ablation layer form characteristic peaks on the depth-profiling curve. A systematic shift of these peaks towards lower ablation layer numbers is observed while the measurement locations become closer to the centre of the inclusion, as indicated by the arrows in Fig. 4, (b, c and d). This shift is likely due to measurement of the same assembly of dark needles embedded in the matrix with a certain angle to the surface normal. The closer one gets to the centre of the

dark inclusion, the earlier one measures the needle assembly because the darker area is closer to the surface and the needles were growing in opposite direction, along the direction of depth of the thin section. Figure 4 (panels' from e to h) displays the mass peak intensity correlations of C with Ca, and O with Ca, measured at locations from 5 to 8. At location 5, the mass peak intensities correlate linearly well and only a small group of data points lay outside the correlation line. Contrary, at location 6, the linear correlation is observed only for a small part of data points (panel f). At locations 7 and 8, no obvious linear correlation can be observed; the data points form a diffuse distribution with a large intensity spread. The data points in the depth profiles measured in locations 5 and 6 (Fig. 4, panels' a and b, respectively), for which the calcium carbonate mineral was identified via the linear correlations (red and black data points on the linear regression in panels e and panel f) are indicated as green circles in panels' a and b, respectively. These are found at the ablation layer numbers between regions of increased peak intensities on the depth-profiling curve. These layers with calcium carbonate, if present, are not easy to detect at locations 7-9. By fitting the fraction of the data that correlates to the calcium carbonate mineral at location 6, one obtains slope coefficient values for O, which are larger compared to that determined at the location of a pure calcium carbonate. The slope coefficient values in correlation of C and Ca are observed to be similar to each other at these locations. With the slope coefficient values of 0.41 ± 0.06 and 0.31 ± 0.02 (location 6), one can derive RSC of O and C 0.13 ± 0.06 and 0.31 ± 0.02 , respectively. RSC for Ca is chosen as the reference and is equal 1. These values will be corrected further using the RSC results determined on oxides and sulphides by taking RSC of Fe as reference.

Depth profiles at location 9

Figure 5 shows depth profiles of several major and minor elements recorded at location 9. Significant mass peak intensity variations for all elements can be observed along the depth profiles at specific ablation layer numbers. Signal intensity variations indicate either a deficit or an increase of the element concentration at

these specific ablation layers. Some increase of the ablation efficiency can occur because of the increased laser radiation absorption at darker spots such as needles. In agreement with the signal intensity correlation studies at locations 7 and 8, we also observe that the Ca, C, and O signals do not correlate linearly. Moreover, at certain depths, a depletion of Ca is observed shown as shaded areas in Fig. 5a. At the ablation layers 53:58, 65:71, 128:132, 156:161, and 165:171, one can observe that the K intensity drop is accompanied by an increase of the intensities of Na, C, and Ca (Fig. 5 a). Considering correlations of the minor elements, an increase of the S, Ni, Co, Mg, Mn, Cu, and B at several locations is typically accompanied by a decrease of the Fe and Ti mass peak intensities (see shaded areas in Fig. 5b and Fig. 5c). Only at the ablation, layer 110 all peaks intensities are observed to correlate. From the microscope images of the needle-like structures one can estimate their size to be in the range of $0.8 - 2 \mu\text{m}$ (Fig. 1b). The narrowest peaks in the depth profile involve 5 ablation layers (see Fig. 5). Thus, the thickness of the measured individual ablation layers is estimated to be in a range $0.2 - 0.4 \mu\text{m}$.

Determination of RSCs from the data collected at locations 6 to 9

If the atomic signals were measured stoichiometric, the slope in the correlation would represent the abundance ratios of the elements of the relevant chemical formula. So far, we have determined RSCs for the elements C and O through their abundance correlation with Ca. Based on our previous studies we know that in the inclusion material other small chemical compounds are present including oxides and sulphides. By correlating the intensities of other elements with oxygen and sulphur intensities, one can gain the information about the RSCs for these elements providing that they form oxides and/or sulphides.

In Figure 6, the intensities of several elements are set in correlation with S (left panel) and O (right panel) intensities, respectively. For some parts of the data set, a linear correlation, either with oxygen or sulphur is observed indicating that these elements may have their origin in oxides and/or sulphides. This agrees with the

coefficient values for the red and blue slope are 1.4 ± 0.1

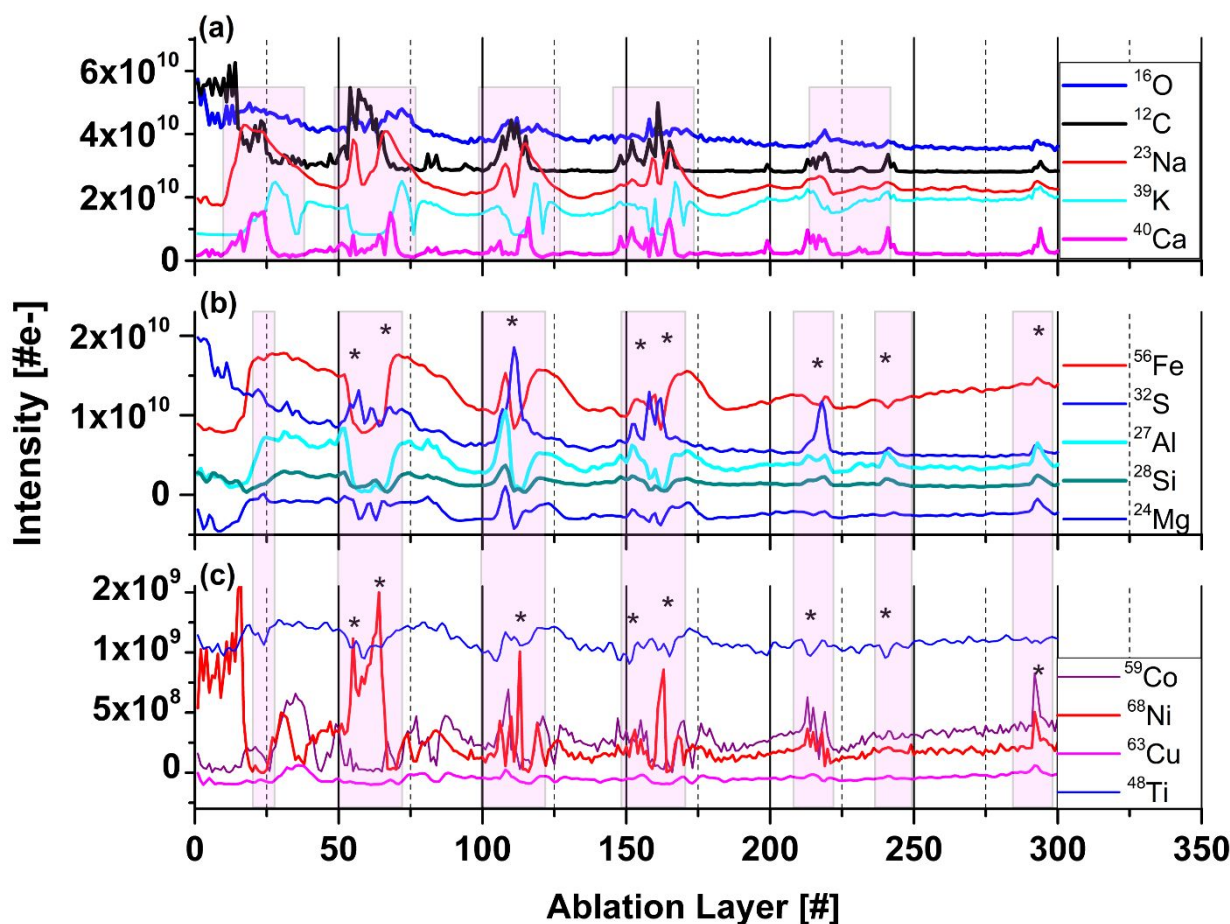


Fig. 5 Variation of the intensities as function of ablation layer number for several elements (isotopes) measured on the dark inclusion at location 8 (Fig. 1b). Panel (a) shows the intensity variations of the C, O, Ca, Na, and K intensities. Panel (b) shows variations of the Fe, S, Mg, Al, and Si intensities. Panel (c) shows variations of Ti, Ni, Co, and Cu intensities. At ablation layers marked by (*) the intensities of these elements correlate well with S, and anticorrelate with Fe. Shaded area highlights layer with specific element correlation, respectively anticorrelations. The traces are shifted to each other vertically for better visualisation of their shapes.

results of our earlier studies, where identification of oxides and sulphides with other analytical methods were performed⁶. Typically, the fs-LIMS measurements on Standard Research Materials show that RSCs for almost all metallic elements are, generally, close to one within about 15%. An exception are Al, Ti, Cu and Mg. RSCs of non-metallic elements such as C, S, O, Si and Ca various within broader range and depends sensitively on the ablation conditions and material properties^{18, 21}.

Iron is an abundant element in the inclusion. Typically, iron occurs ubiquitously in hydrothermal ore deposits in sulphides, oxides, silicates, and in carbonate minerals. In the correlation of the Fe with O intensities, we observe three different linear slopes (Fig. 6d). The

and 3.3 ± 0.3 , respectively. RSC value for Fe is typically close to 1 (in most cases within 15% uncertainty) as it can be determined in the analyses of various materials including metallic or rock samples^{18, 21, 47}. With RSC of Fe equal to 1 one, we derive RSC of O equal 0.3 ± 0.03 considering chemical formulas FeO for blue slope. The slope coefficient of the red slope is 1.4, which is sufficiently close to 1.6 as one would expect for FeO₂ (Fig. 6 panel d). The most common oxidation states of Fe are, however, +2 and +3. With these valences Fe can be found in minerals such FeO (ferric oxide), Fe₂O₃ (Hematite) or Fe₃O₄ (Magnetite). Thus, the FeO₂ compound with oxidation state 4 is unlikely to occur in our sample. Most viable candidate instead of FeO₂ can

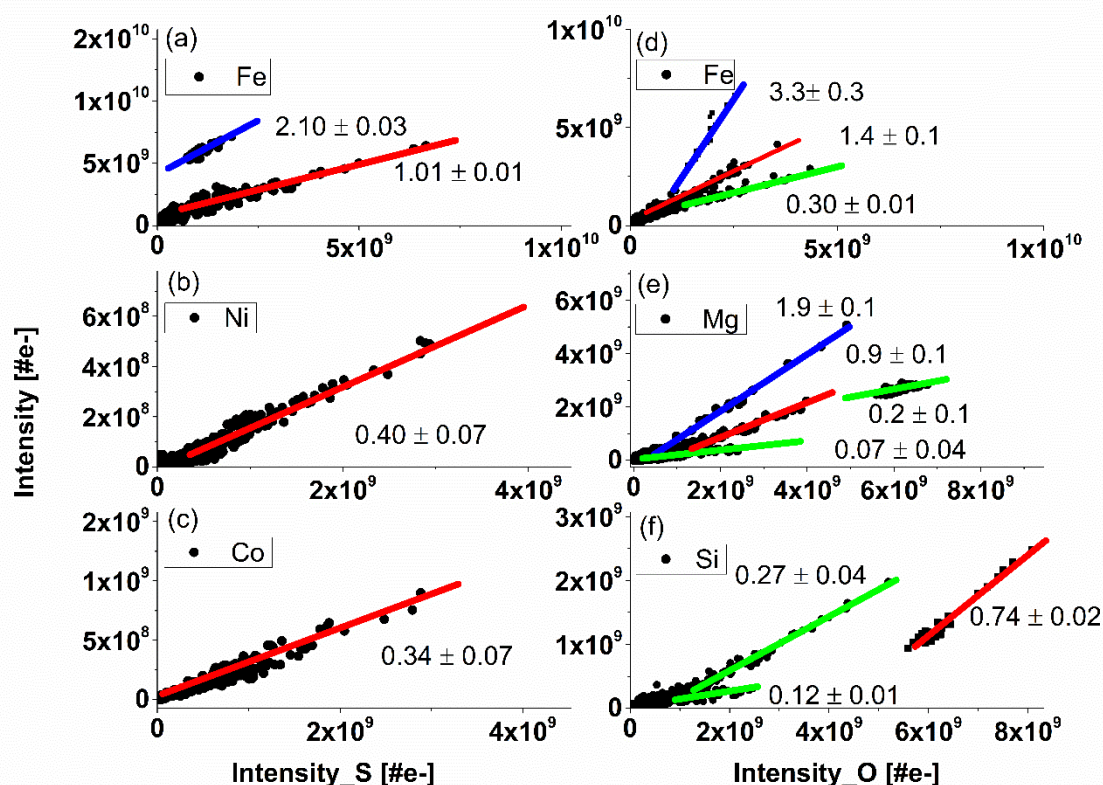


Fig. 6 The correlation of Fe, Ni, and Co with S (panels a-c), and the correlation of Fe, Mg, and Si with O (panels d-f) based on all data measure on locations 6 to 9 (see Fig. 1b). The y-axis represents the intensity of the indicated element in the legend. The slopes (blue) are given for each correlation curve for the oxides and sulphides. RSCs are determined from the blue slopes. Lower slope values than expected for sulphides and oxides indicates that the analysed element was within another compound or a more complex.

be iron (II) hydroxide or ferrous hydroxide with the formula $\text{Fe}(\text{OH})_2$. Ferrous hydroxide is produced when iron(II) salts, e.g., iron(II) sulfate is treated with hydroxide ions. This process is likely to occur in aqueous environments including hydrothermal systems⁴⁸. The slope coefficient of the third correlation of Fe with O observed in Fig. 6c is smaller than the one assigned to the oxides. This result implies that those measured atomic signals may originate from more complex mixture of relevant chemical compounds or mineral phases. With RSC value of O obtained here, we can scale now RSCs of C and Ca determined at the location 6. With RSC of O equal 0.3, RSCs of C and Ca are 0.62 and 2, respectively.

In similar analysis conducted for the correlation of Fe with S, two linearly correlated populations are observed (Fig. 6a). Taking the RSC value of Fe as 1 again, one can

now determine the RSC value of S. The two correlation curves give the correlation coefficients 2.10 ± 0.03 (blue) and 1.01 ± 0.01 (red), respectively. Assigning the blue and red slopes as being due to the FeS and FeS_2 compounds, respectively, one can derive RSC of S equal to 0.48 ± 0.01 . The FeS and FeS_2 are the most common forms of iron sulfides known in natural environments, such as Mackinawite (metastable form of FeS , pyrrhotite (thermodynamically more stable form of FeS), cubic FeS , (formed in presence of foreign ions e.g. chloride ions), and pyrite (FeS_2). These compounds are formed frequently in hydrothermal environments. In our previous study, no pyrite could be identified in the inclusion though this compound is the most important sulphide gangue mineral and occurs in virtually all major hydrothermal base and precious metal mineral deposits. Nevertheless, if the deposits are subjected to high-grade metamorphism, pyrrhotite (FeS) replaces pyrite. This

occurs typically by dissolution of pyrite from aqueous solutions^{49, 50}. Hence, the chemical formula $\text{Fe}(\text{SH})_2$ is suggested instead FeS_2 to be present in the inclusion⁴⁸.

The slope coefficients of the Ni S, and Co and S correlation curves are 0.34 ± 0.07 and 0.4 ± 0.07 , respectively, yielding RSCs of Co and Ni equal to 0.7 ± 0.1 and 0.8 ± 0.1 , respectively. These coefficients are somewhat too small to yield expected chemical formula NiS and CoS, providing that RSCs of these elements are typically close to one^{21, 47}. One of the reason for this can be that the compounds NiS and CoS are well mixed and effectively a (Ni, Co)S compound is sampled in our experiment. To satisfy the chemical formula one needs to sum up the contributions from the Ni and Co atomic signals at the measurement location. The determination of RSC for S (from Fe-sulphides) also allows to conclude that the size of the other Ni and Co sulphides inclusions are smaller than the ablated layer thickness (~ 150 nm). The ablation layers where NiS and CoS are measured cannot be resolved to see separate compounds. The optical imaging of the inclusion area shows large density of needles characteristic of millerite mineral⁶. In addition to Co, also Cu, Mn, and Fe are known impurities, which are identified in millerite. Figure 5 shows that at the ablation layers at which an increase of the Ni, Co and S signals is observed also signals of Mn, Cu or Mg increases. An exception are Fe and Ti signals, which decrease for these specific ablation layers. Also for Ni and Co intensities correlations with O, the slopes coefficients are observed to be too small.

For the Mg and O intensity correlation, we observe four slopes and with S one slope. The slope with the coefficient 1.9 ± 0.1 corresponds likely to MgO. With RSC of O equal to 0.3, RSC of Mg equal to 0.58 is derived. The correlation slope coefficient 0.91 ± 0.06 indicates that MgO_2 could be present in the inclusion. Again, in this case similarly to other above cases, it is more likely that $\text{Mg}(\text{OH})_2$ is present instead. The Mg and O intensity correlation yields the slope coefficient of 0.94 ± 0.03 and RSC of Mg equal to 0.45, hence, close to the value 0.58, determined from the correlation slope of MgO. Thus, the slope value is consistent with the measurement on MgS.

Three linear correlations of Si with O are observed. Quartz (SiO_2) is typically, the gangue mineral, most commonly encountered in ore-forming hydrothermal systems. Considering slope coefficient 0.74 and RSC of O equal to 0.3 determined earlier by correlating Fe and O signals, one can derive RSC of Si equal to 0.22. The correlation curves with smaller slope coefficients can reflect the presence of other mineralogical phases with a lower Si fraction in the compound.

A small part of data points of Ti are observed to linearly correlate with the slope coefficient 0.22 ± 0.03 indicating that Ti may be a part of more complex mineralogical phase.(Fig. 5, panel c). In the analysed locations on the inclusion there is also no correlation of Ti with O observed. TiO_2 (anatase mineral) was identified, however, in the previous studies in other inclusion locations. The Al with O intensity correlation yield the slope coefficient of 0.9 ± 0.1 . Aluminium oxide (Al_2O_3 , alumina) occurs naturally. Again, considering RSC of O 0.3 we derive RSC of Al equal to 0.4 ± 0.1 . For the other trace elements including B, V, Cr, Mn, Zn and Cu measured here the correlation curves are too diffuse and the linear fit is not applied. However, their RSCs are expected to be close to one^{17, 19, 47}. The RSCs for non-metals such as Si, C, O, S or P are typically smaller than one. RSCs of Na and K are typically larger than 1, because it is relatively easy to ionise alkali elements. RSCs of Na and K could not be derived from the correlation of these elements with O or S. For the minor and trace elements, the measurement intensities have larger statistical fluctuations resulting in less accurate determination of the slope coefficients. There are ablation layers in which the relevant atomic signals are weak or not detectable. For too large signals, the mass peak intensities can be under-measured due to the detector saturation effects. For large differences in material properties from one ablation layer to the other, the ablation process and efficiency of ion production may change affecting linearity of the atomic intensity correlation. The effects affecting the mass peak intensity measurements are discussed in more detail in our recent publication⁵¹. The RSCs of investigated elements are summarised in Table 1.

Table 1: Relative sensitivity coefficients (RSCs) determined from the intensity correlations (see Figs. 4 and 6). RSCs larger and smaller than 1 indicate larger and lower than expected atom ionisation efficiencies, respectively. The relative statistical errors of the RSC determination are typically within a few per cent. The RSC coefficients determined on oxides and sulphides can have uncertainty of about 20 % (see text for the details).

Element	RSC	Element	RSC
C	0.6	Ti	0.1 observed 1-1.5 expected
O	0.3	Fe	1
Ca	2	Mg	0.6
Si	0.2	Ni	0.8, observed 1 expected
S	0.5	Co	0.7 observed 1 expected
Al	0.4	Na, K	>1 expected

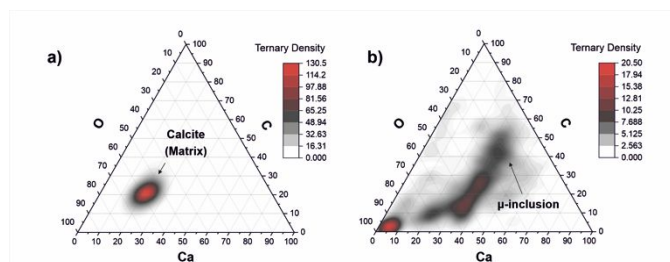


Fig. 6 Ternary diagram of the C, O, and Ca concentration fractions with applied RSCs that were derived on a pure calcium carbonate phase at location 1-4. (a) and on the dark inclusion (b) at locations from 6 to 9. Only a part of the data points in panel (b) can be assigned to calcium carbonate mineral. On the O axes the 3 times O concentration is applied thus the fractions of C, Ca and 3O are the same for carbonate mineral and experimental points are in the middle area in the triangle. The other remaining points indicate presence of other mineralogical compounds.

Mineralogical phases

Calcium carbonate

Ternary plots are frequently used in the mineralogical analysis in geology. They can be helpful in identification of the mineralogical context of the analysed sample just by applying a minimum number of chemical species, which are necessary to describe the composition. In the conventional analysis of carbonate phases, ternary diagram correlating abundance fractions (Ciderite-Magnesite-Calcite) is applied. For pure calcium carbonate, the ternary plot of the C, O, and Ca abundance fractions is shown in Fig. 7, panel a. The

experimental data points are observed to be located close to each other, with element abundance ratios (atomic fractions, 20:20:60:) that agrees with the chemical formula CaCO_3 . Contrary, the plot of the data representing the measurements on locations 6 to 9 shows very diffuse distribution with large spread from the area expected for the calcite mineral (Fig. 7, panel b). This may indicate that the other minerals instead a calcium carbonate are present at the inclusion location. This goes along with our previous investigations with spectroscopic methods, which identified the presence of mineralogical phases such as clinochlore $[(\text{Mg}_5\text{Al})(\text{AlSi}_3\text{O}_{10})(\text{OH})_8]$, clinochlore-transformed augite $(\text{Ca}, \text{Na})(\text{Mg}, \text{Fe}, \text{Al}, \text{Ti})(\text{Si}, \text{Al})_2\text{O}_8$ and plagioclase (feldspar group) $[\text{NaAlSi}_3\text{O}_8\text{-CaAl}_2\text{Si}_2\text{O}_8]$.

Clinochlore, Pyroxene-Augite, Plagioclase

Clinochlore is a member of chlorite group of phyllosilicate minerals and often contains considerable amounts of Fe^{2+} , grading into chamosite. Clinochlore is described by the chemical formula $\text{Mg}_5\text{Al}(\text{AlSi}_3\text{O}_{10})(\text{OH})_8$, and Fe, Mn, Zn, Ca, and Cr are common impurities. Figure 8a shows the ternary plot of the Mg, Al, and Fe element abundances to illustrate their relative proportions measured in the dark inclusion (Fig. 1b). These proportions indicate that the clinochlore mineral is a major mineral in the dark inclusion with the average $\text{Mg}/(\text{Mg}+\text{Fe})$ abundance ratio of $\sim 0.34 \pm 0.14$. Within ultramafic rocks, metamorphism produces predominantly clinochlore chlorite, an Mg-rich end member, which could be identified as the inclusion.

Clinochlore-transformed augite mineral is a member of pyroxene group namely calcic clinopyroxenes (diopside, hedenbergite, augite). Pure diopside of $\text{CaMgSi}_2\text{O}_6$ chemical composition can undergo as a complete solid solution to hedenbergite $\text{CaFeSi}_2\text{O}_6$ or augite $(\text{Ca}, \text{Mg}, \text{Fe}^{2+}, \text{Fe}^{3+}, \text{Al})_2(\text{Si}, \text{Al})_2\text{O}_6$. In another chemical formula proposed for pyroxene group $(\text{Ca}_x\text{Mg}_y\text{Fe}_z)(\text{Mg}_{y1}\text{Fe}_{z1})\text{Si}_2\text{O}_6$, for augite, the relative composition of Ca can vary within the range $0.4 \leq x \leq 0.9$ where $x+y+z=1$ and $y_1+z_1=1$ ⁵². The ternary plot of Mg, Fe, and Ca proportions indicates presence of magnesian augite in the inclusion material (Fig. 8b).

Figure 8c shows the ternary diagram of the phases around the millerite needles. Oxides and

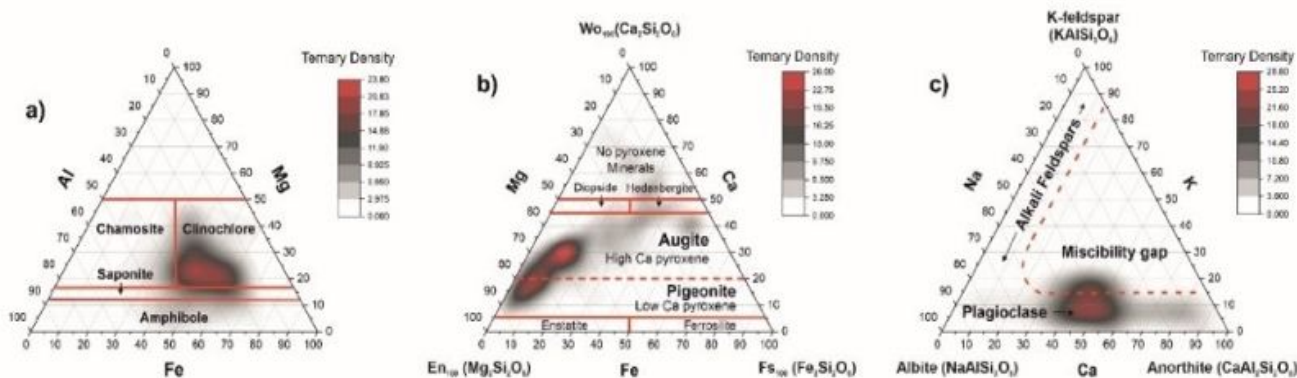


Fig. 8 Ternary plots of the elements relevant to chlorite and feldspar groups. (a): The correlation of the Al, Mg, and Fe abundances showing characteristic regions for various minerals of the chlorite group; (b): The correlation between the Mg, Fe, and Ca abundance ratios indicating the presence of magnesium augite and pigeonite in the sample material; (c): The correlation diagram of the Ca, K, and Na elements indicate the presence of the plagioclase feldspars in the inclusion material.

abundances of the elements K, Na, and Ca, which is applied for the classification of feldspar minerals. One can identify the distribution of data along the base of the K coordinate, and the miscibility gap in the centre. The sequence of minerals along the base of the triangle indicate the presence of the plagioclase mineral or the solid solution series of plagioclase being a mixture between albite (sodium aluminosilicate: $[\text{Na}(\text{AlSi}_3\text{O}_8)]$) and anorthite (calcium aluminosilicate: $[\text{Ca}(\text{Al}_2\text{Si}_2\text{O}_8)]$) and the notable absence of alkali feldspars⁵³. The red line denoting location of the feldspars is schematic. The RSC values of K and Na are chosen 1, which can be the reason that we observe the plagioclase on ternary diagram shifted more in the alkali region. The RSCs of K and Na are expected to be larger than 1 but they cannot here be derived accurately using the abundance correlation method applied to simple compounds.

In our previous studies the analyses conducted by various analytical techniques showed that the dark inclusion investigated here is highly weathered basalt with olivine, and pyroxene (augite) phenocrysts with a dominating amygdales phase⁶. Typically, amygdales in basaltic lavas are formed after lava cools down, and hydrothermal fluids pass through the cavities. Their precipitation in the bubbles form secondary minerals such as calcium carbonate, zeolites, and quartz, depending on the fluid composition. The depth profiles indicate also presence of layers of various mineralogical

sulphides of several metals are present as separate entities and some of the metals fill the sites of complex mineralogical compounds⁴⁸.

Summary

We describe the mass spectrometric measurements conducted by fs-laser ablation/ionisation time-of-flight mass spectrometry and introduce principles of data analysis, which yields to true elemental abundances. The corrections to measured atomic abundances are obtained by analysing atomic intensity correlations using depth-profiling data. In heterogeneous sample such as analysed inclusion embedded in a calcium carbonate mineral, chemical compounds are present at specific depths and can be identified in specific ablation layers. By correlating the measured atomic intensities, one can select the data points for which atomic intensities, correlate linearly. With the slope coefficients of these correlations, the relative abundances of the correlated elements can be derived. The method was tested initially on a pure calcium carbonate phase followed by locations at the interface between inclusion and calcite mineral and on the inclusion. RSCs for major and minor elements were derived by correlating atomic intensity of these elements with either oxygen or sulphur. Subsequently, with the corrected elemental abundances more complex mineralogical phases were analysed by applying the ternary atomic abundance

fraction correlations on specific elements typically chosen in geological analysis of the mineralogical context.

The mass spectrometric results are consistent with the results presented in our former studies of this sample conducted with several other instruments. However, LIMS studies cannot differentiate between minerals with the same chemical formula such as calcium carbonate mineral, which can occur as aragonite, calcite or vaterite. To conduct such analysis the Raman measurements will be necessary. Similarly, with the IR analysis one would approve our ambiguous assignment of presence of hydroxides or hydrosulphides in the sample. The presented method can be important in studies of highly heterogeneous materials, because matrix-matched reference materials are often not available for complex natural samples. The in situ determined RSCs can overcome the problems associated with the local heterogeneity, which can occur in the micrometre range similar to the sample probing laser spot. Thus, the in situ atomic abundance calibration introduced here can allow quantitative chemical composition investigation of heterogeneous structures. With the detection of heterogeneity in the micrometre scale, one can analyse grain-size objects such as micro-sized minerals or microfossils in detail. The presented method can be also of interest in searches for ancient fossilised life forms on planetary surfaces because in addition to context mineralogy, high depth profiling resolution provides means for isolation and analyses of microfossils embedded in mineralogical phases.

Acknowledgments

P. Wurz acknowledges financial support by Swiss Science Foundation (SNSF). Dr. Sean McMahon is acknowledged for providing us the sample we analysed in the current studies.

References

1. K. E. Peters, J. M. Walters and J. M. e. Moldowan, *The Biomarker Guide*, Cambridge University Press, 2005.
2. A. H. Stevens, A. McDonald, C. de Koning, A. Riedo, L. J. Preston, P. Ehrenfreund, P. Wurz and C. S. Cockell, *Sci Rep-Uk*, 2019, **9**.
3. A. Riedo, C. de Koning, A. Stevens, A. C. o. L. p. McDonald, A. M. Tulej, P. Wurz, C. S. Cockell and P. Ehrenfreund, *Astrobiology*, 2020, **accepted**.
4. J. M. Reess, M. Bonafous, L. Lapauw, O. Humeau, T. Fouchet, P. Bernardi, P. Cais, M. Deleuze, O. Forni, S. Maurice, S. Robinson, R. C. Wiens and S. Team, *Proc Spie*, 2018, **11180**.
5. P. Sarrazin, D. Blake, M. Gailhanou, F. Marchis, C. Chalumeau, S. Webb, P. Walter, E. Schyns, K. Thompson and T. Bristow, *J Instrum*, 2018, **13**.
6. A. Neubeck, M. Tulej, M. Ivarsson, C. Broman, A. Riedo, S. McMahon, P. Wurz and S. Bengtson, *International Journal of Astrobiology*, 2016, **15**, 133-146.
7. M. Tulej, A. Riedo, M. B. Neuland, S. Meyer, P. Wurz, N. Thomas, V. Grimaudo, P. Moreno-Garcia, P. Broekmann, A. Neubeck and M. Ivarsson, *Geostand Geoanal Res*, 2014, **38**, 441-466.
8. M. Tulej, A. Neubeck, M. Ivarsson, A. Riedo, M. B. Neuland, S. Meyer and P. Wurz, *Astrobiology*, 2015, **15**, 669-682.
9. Y. M. Lin, Q. A. Yu, W. Hang and B. L. Huang, *Spectrochim Acta B*, 2010, **65**, 871-883.
10. A. A. Sysoev and A. A. Sysoev, *Eur J Mass Spectrom*, 2002, **8**, 213-232.
11. A. A. Sysoev, A. V. Karpov, V. V. Milyaeva and A. A. Sysoev, *Eur J Mass Spectrom*, 2018, **24**, 96-107.
12. U. Rohner, J. A. Whitby and P. Wurz, *Meas Sci Technol*, 2003, **14**, 2159-2164.
13. M. Tulej, M. Iakovleva, I. Leya and P. Wurz, *Anal Bioanal Chem*, 2011, **399**, 2185-2200.
14. A. Riedo, A. Bieler, M. Neuland, M. Tulej and P. Wurz, *J Mass Spectrom*, 2013, **48**, 1-15.
15. R. Wiesendanger, M. Tulej, A. Riedo, S. Frey, H. Shea and P. Wurz, *J Anal Atom Spectrom*, 2017, **32**, 2182-2188.
16. R. Wiesendanger, D. Wacey, M. Tulej, A. Neubeck, M. Ivarsson, V. Grimaudo, P. Moreno-Garcia, A. Cedeno-Lopez, A. Riedo and P. Wurz, *Astrobiology*, 2018, **18**, 1071-1080.
17. J. He, R. F. Huang, Q. Yu, W. Hang and B. L. Huang, *Chem J Chinese U*, 2009, **30**, 57-59.
18. B. C. Zhang, M. H. He, W. Hang and B. L. Huang, *Anal Chem*, 2013, **85**, 4507-4511.
19. S. D. Zhang, B. C. Zhang, W. Hang and B. L. Huang, *Spectrochim Acta B*, 2015, **107**, 17-24.
20. Z. B. Yin, L. Hang, R. Liu, W. Hang and B. L. Huang, *J Mass Spectrom*, 2018, **53**, 435-443.
21. A. Riedo, M. Neuland, S. Meyer, M. Tulej and P. Wurz, *J Anal Atom Spectrom*, 2013, **28**, 1256-1269.
22. V. V. Milyaeva, E. E. Sil'nikov, A. M. Mikhailov and A. A. Sysoev, *Eur J Mass Spectrom*, 2017, **23**, 167-173.
23. M. Tulej, R. Wiesendanger, A. Riedo, G. Knopp and P. Wurz, *J Anal Atom Spectrom*, 2018, **33**, 1292-1303.
24. R. F. Huang, Y. M. Lin, L. F. Li, W. Hang, J. He and B. L. Huang, *Anal Chem*, 2010, **82**, 3077-3080.
25. R. Wiesendanger, V. Grimaudo, M. Tulej, A. Riedo, R. Lukmanov, N. Ligterink, R. Fausch, H. Shea and P. Wurz, *J Anal Atom Spectrom*, 2019, **34**, 2061-2073.
26. M. B. Neuland, S. Meyer, K. Mezger, A. Riedo, M. Tulej and P. Wurz, *Planet Space Sci*, 2014, **101**, 196-209.
27. S. Frey, R. Wiesendanger, M. Tulej, M. Neuland, A. Riedo, V. Grimaudo, P. Moreno-Garcia, A. C. Lopez, M. Mohos, B. Hofmann, K. Mezger, P. Broekmann and P. Wurz, *Planet Space Sci*, 2020, **182**.

Journal Name

- 1
2
3 28. A. Riedo, M. Tulej, U. Rohner and P. Wurz, *Rev Sci Instrum*,
4 2017, **88**.
- 5 29. V. Grimaudo, P. Moreno-Garcia, A. C. Lopez, A. Riedo, R.
6 Wiesendanger, M. Tulej, C. Gruber, E. Lortscher, P. Wurz
7 and P. Broekmann, *Anal Chem*, 2018, **90**, 5179-5186.
- 8 30. V. Grimaudo, P. Moreno-Garcia, A. Riedo, M. B. Neuland,
9 M. Tulej, P. Broekmann and P. Wurz, *Anal Chem*, 2015, **87**,
2037-2041.
- 10 31. V. Grimaudo, M. Tulej, A. Riedo, R. Lukmanov, N. F. W.
11 Ligterink, C. de Koning and P. Wurz, *Rapid Commun Mass*
12 *Sp*, 2020, **34**.
- 13 32. V. Grimaudo, P. Moreno-Garcia, A. Riedo, S. Meyer, M.
14 Tulej, M. B. Neuland, M. Mohos, C. Gutz, S. R. Waldvogel,
15 P. Wurz and P. Broekmann, *Anal Chem*, 2017, **89**, 1632-
16 1641.
- 17 33. M. H. He, Y. F. Meng, S. S. Yan, W. Hang, W. G. Zhou and B.
18 L. Huang, *Anal Chem*, 2017, **89**, 565-570.
- 19 34. B. Fernandez and R. Pereiro, *Anal Bioanal Chem*, 2010, **396**,
20 2723-2724.
- 21 35. B. Fernandez, R. Pereiro and A. Sanz-Medel, *Anal Chim*
22 *Acta*, 2010, **679**, 7-16.
- 23 36. B. Hattendorf, J. Pisonero, D. Gunther and N. Bordel, *Anal*
24 *Chem*, 2012, **84**, 8771-8776.
- 25 37. A. Pelster, M. Korsgen, T. Kurosawa, H. Morita and H. F.
26 Arlinghaus, *Anal Chem*, 2016, **88**, 9638-9646.
- 27 38. J. Pisonero, *Anal Bioanal Chem*, 2006, **384**, 47-49.
- 28 39. J. Pisonero, J. Koch, M. Walle, W. Hartung, N. D. Spencer
29 and D. Gunther, *Anal Chem*, 2007, **79**, 2325-2333.
- 30 40. M. Ivarsson, *Biogeosciences*, 2012, **9**, 3625-3635.
- 31 41. M. Ivarsson, W. Bach, C. Broman, A. Neubeck and S.
32 Bengtson, *Geomicrobiol J*, 2018, **35**, 460-467.
- 33 42. M. Ivarsson, S. Bengtson, V. Belivanova, M. Stampanoni, F.
34 Marone and A. Tehler, *Geology*, 2012, **40**, 163-166.
- 35 43. S. McMahon, T. Bosak, J. P. Grotzinger, R. E. Milliken, R. E.
36 Summons, M. Daye, S. A. Newman, A. Fraeman, K. H.
37 Williford and D. E. G. Briggs, *J Geophys Res-Planet*, 2018,
38 **123**, 1012-1040.
- 39 44. S. McMahon, J. Parnell and N. J. F. Blamey, *International*
40 *Journal of Astrobiology*, 2012, **11**, 163-167.
- 41 45. R. Wiesendanger, M. Tulej, V. Grimaudo, A. C. Lopez, R.
42 Lukmanov, A. Riedo and P. Wurz, *Journal of Chemometrics*,
43 2018, DOI: 10.1002/cem.3081, 1-10.
- 44 46. S. Meyer, A. Riedo, M. B. Neuland, M. Tulej and P. Wurz, *J*
45 *Mass Spectrom*, 2017, **52**, 580-590.
- 46 47. M. B. Neuland, V. Grimaudo, K. Mezger, P. Moreno-Garcia,
47 A. Riedo, M. Tulej and P. Wurz, *Meas Sci Technol*, 2016, **27**.
- 48 48. T. M. Seward, A. Williams-Jones and A. Migdisov, in *Tratise*
49 *on Geochemistry*, Elsevier Ltd., 2013, vol. 13.
- 50 49. U. M. Graham and H. Ohmoto, *Geochim Cosmochim Ac*,
51 1994, **58**, 2187-2202.
- 52 50. H. Ohmoto, K. Hayashi and Y. Kajisa, *Geochim Cosmochim*
53 *Ac*, 1994, **58**, 2169-2185.
- 54 51. M. Tulej, A. Neubeck, A. Riedo, R. Lukmanov, V. Grimaudo,
55 N. Ligterink, M. Ivarsson, W. Bach and C. de Koning, *J Mass*
56 *Spectrom*, 2020, **accepted**.
- 57 52. N. Morimoto, *Mineral Mag*, 1988, **52**, 535-550.
- 58 53. <http://geology.com/minerals/plagioclase.shtml>).
- 59
60

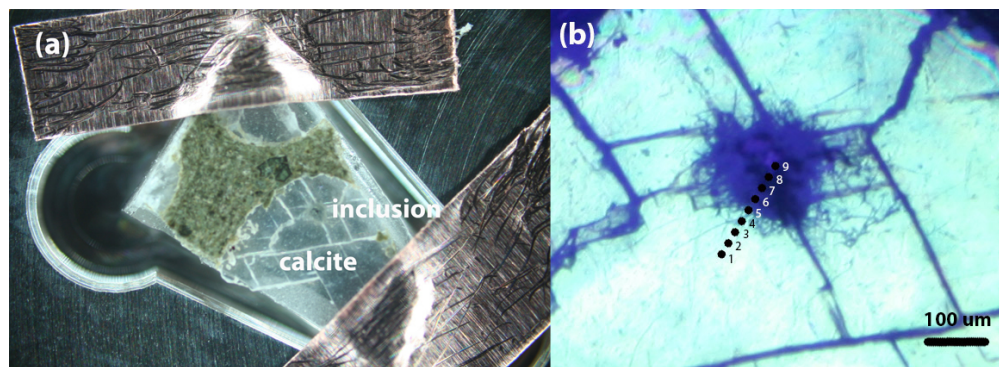


Fig. 1. (a): The sample prior to the introduction into the vacuum chamber. The sample is placed within milled depression in the sample holder made of stainless steel and is attached by a copper tape. (b): Close up microscope image of the amygdale calcium carbonate sample with a dark inclusion in the centre. A network of needle-like structures spreading out from a denser, darker central part of the inclusion can be readily identified. The ten black spots with numbers indicate the location at which laser ablation mass spectrometric analyses were conducted.

409x147mm (72 x 72 DPI)

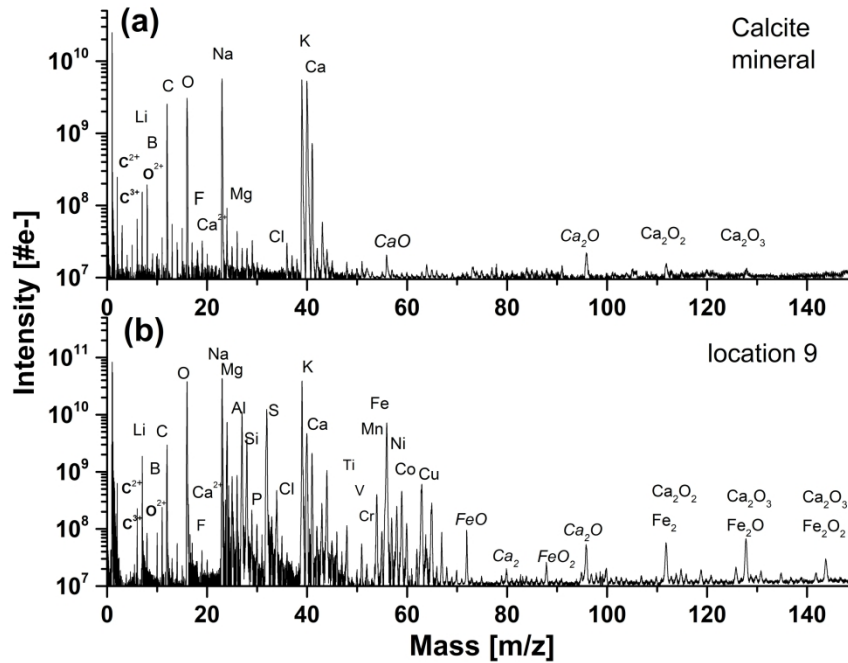


Fig. 2 (a) The mass spectrum recorded on a pure calcium carbonate mineral on location 4, (b) and on the inclusion on location 9.

272x208mm (300 x 300 DPI)

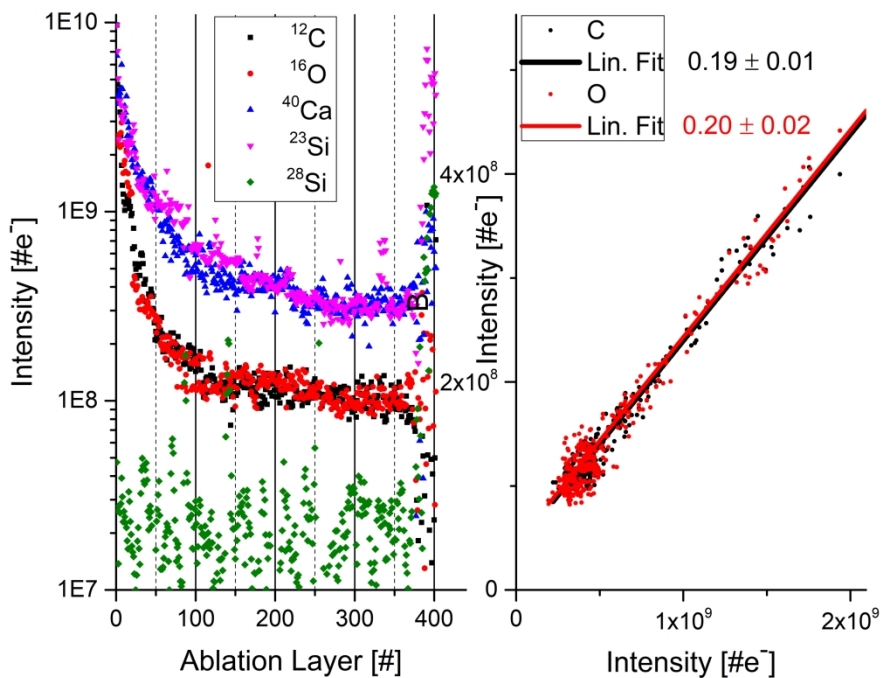


Fig. 3 (a): Depth profile of C, O, Ca, Na, and Si as a function of the ablation number. From the 366 ablation layer one observes an increase of the Si and Na atomic intensities indicating transition to soda lime silica glass substrate material. (b): Correlation between C and Ca, and O and Ca atomic intensities, respectively, derived from the depth profiling data.

272x208mm (300 x 300 DPI)

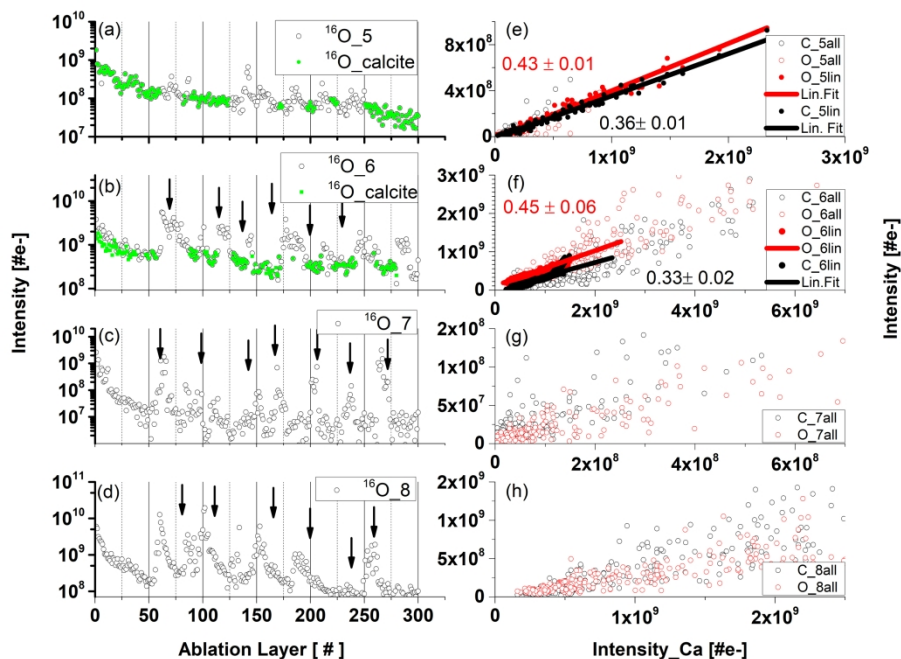


Fig. 4. Depth profiles and mass peak intensity correlations. Panels (a-d): Depth profiles obtained by measuring the O mass peak intensities at the locations 6 panel (b), 7 panel (c), and 9 panel (d) on the dark inclusion. A depth curve on a pure calcium carbonate mineral is added in panel (a) for comparison with depth profiles measured at inclusion locations. The green-coloured points in the left panels are the data points that correspond to the calcium carbonate mineral. Right panels: the correlations of the mass peak intensities of elements C and O (y-axis) with Ca (x-axis) measured at corresponding locations. Only part of the data points correlates linearly (black and red full circles) in panel (f). There was no clear correlation between O and Ca in the data plotted in panel (g), although a C-Ca correlation can be noticed. Contrary, for part of the data points the correlation between O and Ca is readily observed but the correlation between C and Ca is less pronounced in panel (h).

272x208mm (300 x 300 DPI)

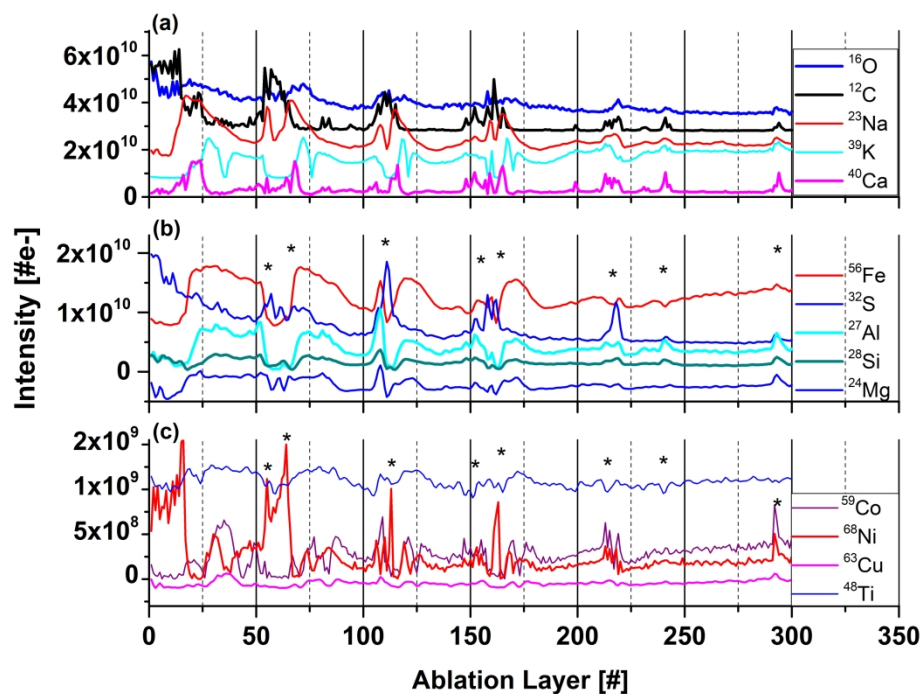


Fig. 5 Variation of the intensities as function of ablation layer number for several elements (isotopes) measured on the dark inclusion at location 8 (Fig. 1b). Panel (a) shows the intensity variations of the C, O, Ca, Na, and K intensities. Panel (b) shows variations of the Fe, S, Mg, Al, and Si intensities. Panel (c) shows variations of Ti, Ni, Co, and Cu intensities. At ablation layers marked by (*) the intensities of these elements correlate well with S, and anticorrelate with Fe. Shaded area highlights layer with specific element correlation, respectively anticorrelations. The traces are shifted to each other vertically for better visualisation of their shapes.

272x208mm (300 x 300 DPI)

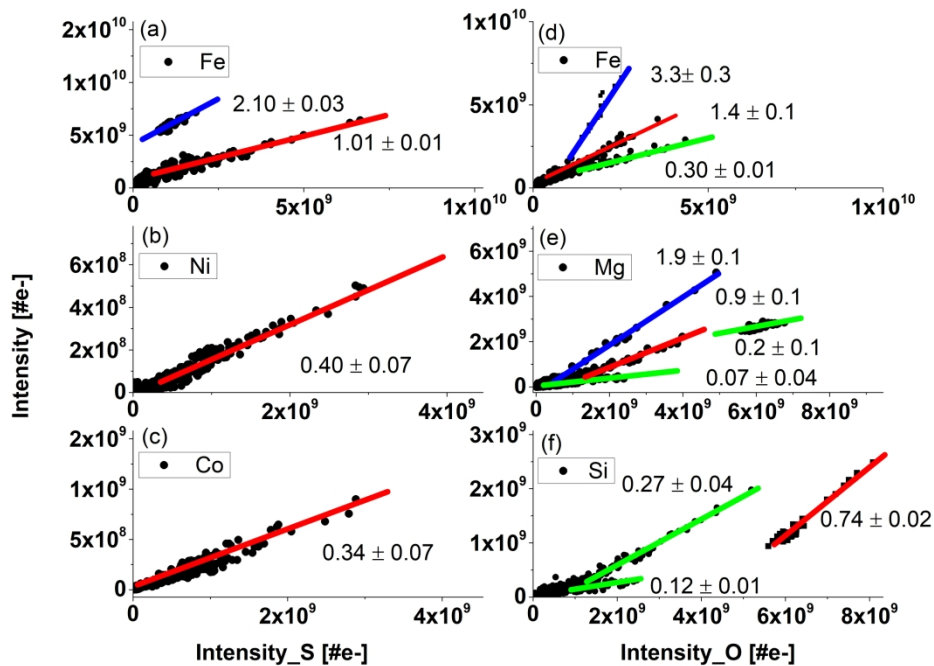


Fig. 6 The correlation of Fe, Ni, and Co with S (panels a-c), and the correlation of Fe, Mg, and Si with O (panels d-f) based on all data measure on locations 6 to 9 (see Fig. 1b). The y-axis represents the intensity of the indicated element in the legend. The slopes (blue) are given for each correlation curve for the oxides and sulphides. RSCs are determined from the blue slopes. Lower slope values than expected for sulphides and oxides indicates that the analysed element was within another compound or a more complex.

272x208mm (300 x 300 DPI)

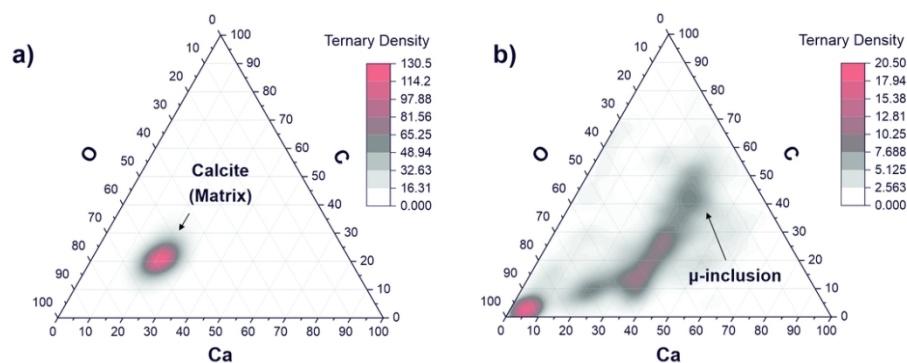


Fig. 7 Ternary diagram of the C, O, and Ca concentration fractions with applied RSCs that were derived on a pure calcium carbonate phase at location 1-4. (a) and on the dark inclusion (b) at locations from 6 to 9. Only insignificant part of the data points in panel (b) can be assigned to calcium carbonate mineral. The other remaining points indicate presence of other mineralogical compounds.

99x38mm (300 x 300 DPI)

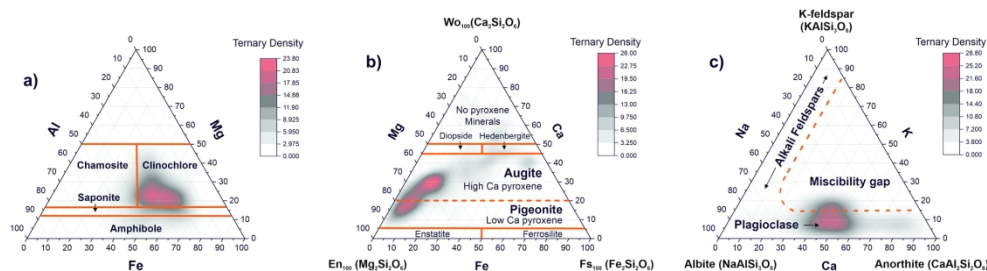


Fig. 8 Ternary plots of the elements relevant to chlorite and feldspar groups. (a): The correlation of the Al, Mg, and Fe abundances showing characteristic regions for various minerals of the chlorite group; (b): The correlation between the Mg, Fe, and Ca abundance ratios indicating the presence of magnesium augite and pigeonite in the sample material; (c): The correlation diagram of the Ca, K, and Na elements indicate the presence of the plagioclase feldspars in the inclusion material.

199x60mm (300 x 300 DPI)

Table 1: Relative sensitivity coefficients (RSCs) determined from the intensity correlations (see Figs. 4 and 6). RSCs larger and smaller than 1 indicate larger and lower than expected atom ionisation efficiencies, respectively. The relative statistical errors of the RSC determination are typically within a few per cent. The RSC coefficients determined on oxides and sulphides can have uncertainty of about 20 % (see text for the details).

Element	RSC	Element	RSC
C	0.6	Ti	0.1 observed 1-1.5 expected
O	0.3	Fe	1
Ca	2	Mg	0.6
Si	0.2	Ni	0.8, observed 1 expected
S	0.5	Co	0.7 observed 1 expected
Al	0.4	Na, K	>1 expected